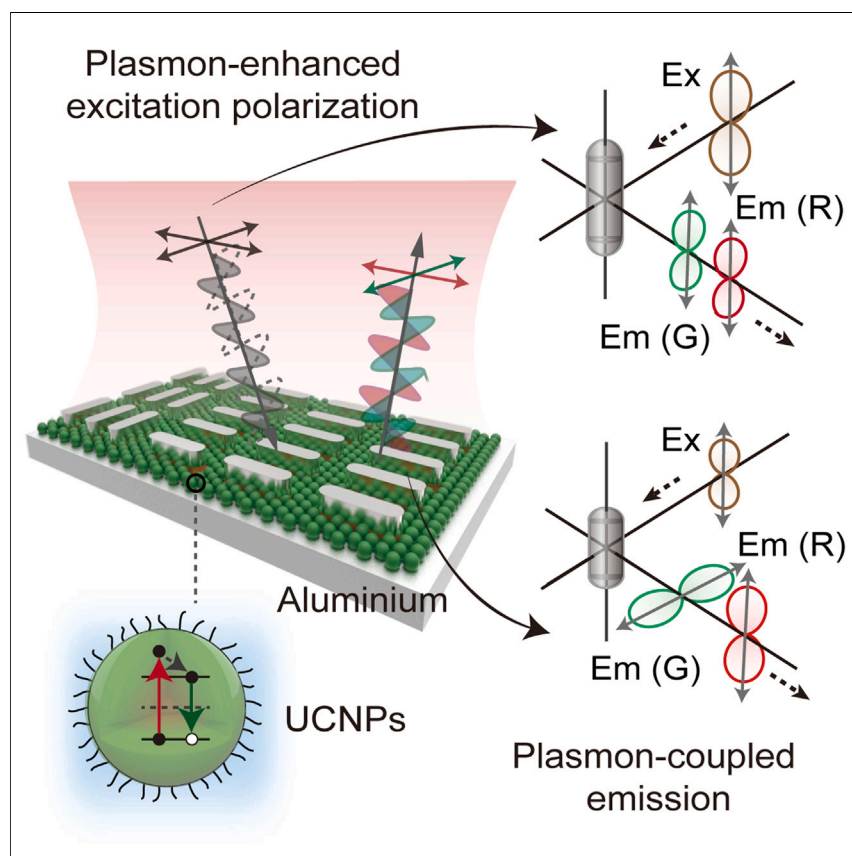


Article

Multi-level upconversion polarization enabled by programmable plasmons



We introduce a platform for upconversion plasmonics that overcomes the limitations of isotropic upconversion nanocrystals by utilizing anisotropic metasurfaces supported by a gap plasmon mode. This platform allows the precise control of plasmon-enhanced excitation polarization and plasmon-coupled emission. When excited with linearly polarized light, the hybrid nanoplatform can toggle between four upconversion polarization states, enabling the generation of multi-level photonic outputs in parallel or orthogonal configurations. Our numerical and experimental results shed light on nonlinear light-matter interactions and luminescence anisotropy at the nanoscale.

Jiahui Xu, Hailong Liu, Hongtao Wang, ..., Joel K.W. Yang, Renaud A.L. Vallée, Xiaogang Liu

renaud.vallee@crpp.cnrs.fr (R.A.L.V.)
chmlx@nus.edu.sg (X.L.)

Highlights

Polarization-controlled upconversion by anisotropic plasmon engineering

Selective polarization modification of excited and radiative dynamics

Programmable nonlinear optical systems with multiple polarization levels

Article

Multi-level upconversion polarization enabled by programmable plasmons

Jiahui Xu,¹ Hailong Liu,² Hongtao Wang,³ Yiming Wu,² Hao Wang,³ Benjamin Yue Hao Tan,² Joel K.W. Yang,³ Renaud A.L. Vallée,^{4,*} and Xiaogang Liu^{1,2,5,*}

SUMMARY

The active control of upconversion polarization in lanthanide-doped nanocrystals through plasmon-photon coupling enables ultra-compact nonlinear photonic devices for polarization-encoded optical communication and information processing. However, current plasmonic nanostructures used for this purpose suffer from limited tunability and insufficient sensitivity to polarization, making effective control challenging. Here, we introduce an upconversion plasmonphore platform that overcomes the limitations of isotropic upconversion nanocrystals by utilizing anisotropic gap-plasmon-mode-supported metasurfaces. This platform allows the precise control of plasmon-enhanced excitation polarization and plasmon-coupled emission. When excited with linearly polarized light, the hybrid nanoplatform can switch between four upconversion polarization states, enabling multi-level photonic outputs in parallel or orthogonal configurations. We also demonstrate an information multiplexing scheme using this platform. Our numerical and experimental results not only shed light on nonlinear light-matter interactions and luminescence anisotropy at the nanoscale but also facilitate the development of novel nonlinear polaritonic nanodevices for polarization-based integrated photonics.

INTRODUCTION

Photon-plasmon coupling in hybrid systems is a powerful tool for investigating light-matter interactions at the nanoscale, with potential applications in various fields, including miniaturized solid-state lasers, ultra-compact spectrometers, on-chip molecular sensing, and polarimetric imaging.^{1–4} Lanthanide-doped upconversion nanoparticles (UCNPs) are particularly promising as quantum light sources due to their distinct emission peaks,^{5–8} large anti-Stokes shift,^{9–11} and excellent photostability.^{12–14} These peaks provide characteristic spectroscopic fingerprints for accurate information identification.^{15–18} Upconversion hybrid systems have been explored to enhance photoluminescence and decay dynamics through surface plasmon-photon coupling.^{19–25} However, the crystal lattice symmetry of small UCNPs makes it difficult to achieve polarization anisotropy, which is crucial for controlling the polarization of upconverted photons.^{26,27}

Current research has investigated the use of plasmonic nanostructures to enhance the polarization sensitivity of UCNPs. The polarization modification of upconversion luminescence can arise from both plasmon-enhanced excitation polarization by the near-field electromagnetic interference and plasmon-coupled emission by radiation engineering. However, modern plasmonic structures suffer from drawbacks, such as

THE BIGGER PICTURE

The control of light polarization is essential for diverse applications, such as information encoding, display technology, and biological sensing. Lanthanide-doped upconversion nanoparticles show promise as quantum light sources for accurate information identification due to their characteristic spectroscopic features. In this work, we demonstrate the precise control of the polarization of isotropic nanoparticles by coupling them with anisotropic gap plasmon modes. By controlling the incident and detection polarization angles in the far field, the hybrid nanoplatform can switch between four upconversion polarization states, enabling parallel or orthogonal photonic outputs. This capability opens up possibilities for programmable nonlinear optical systems with multiple polarization levels. Our investigations provide valuable insights into the design principles for advanced nonlinear quantum systems, offering tailored frequency and polarization behavior at the nanoscale.

inadequate control over resonant mode tuning and insufficient polarization sensitivity, which pose challenges for decoupling multi-upconversion processes and simultaneous manipulation of multiple upconversion transitions.^{28–34} For example, gold nanorods synthesized through wet chemistry exhibit anisotropic plasmonic modes, but it is challenging to achieve a strong resonance along their short axis.^{35,36} Thus far, plasmon-UCNP coupling systems capable of exhibiting programmable, multi-level polarization switching remain unexplored. To overcome these challenges, it is necessary to identify a plasmonic platform that can effectively couple with multiple emissive transitions, while ensuring orthogonal directions for the excitation and emission paths of UCNPs without causing crosstalk between resonant modes. With such a platform, it should be possible to manipulate upconversion polarization states *in situ* and at multiple levels, enabling the development of compact nonlinear photonic devices for information processing and optical communications.

In this work, we demonstrate precise polarization control of isotropic UCNPs by coupling them with anisotropic gap-plasmon-mode-supported metasurfaces (Figure 1A). The metal-insulator-metal (MIM) design facilitates efficient decoupling of excitation and emission dynamics in upconversion processes into orthogonal polarization directions with little crosstalk.³⁷ By tailoring the aspect ratio of antennas, the plasmon wavelength can be tuned across the visible to near-infrared range. Through far-field excitation control, near-field electromagnetic interference modulates the multiphoton population process in a polarization-dependent manner, leading to periodic variations in emission amplitude with a high excitation polarization sensitivity of up to 0.83. Furthermore, we investigate how the local photon densities around antennas influence the radiation field of emitter excitonic energy. By controlling the incidence and detection polarization angles in the far field, the hybrid nanoplatform can switch between four upconversion polarization states, enabling parallel or orthogonal photonic outputs (Figure 1B). This capability opens up possibilities for programmable nonlinear optical systems with multiple polarization levels.

RESULTS AND DISCUSSION

Theoretical consideration

To investigate the effect of anisotropic plasmon resonances on the absorption and emission profiles of adjacent UCNPs, we first developed a model that explicitly describes the dynamics of multiphoton upconversion based on excited-state absorption (ESA) and plasmon field coupling.³⁸ On 980 nm excitation, Er³⁺-activated UCNPs exhibit two characteristic emission bands at around 540 and 655 nm, attributable to the ²H_{11/2}, ⁴S_{3/2} → ⁴I_{15/2}, and ⁴F_{9/2} → ⁴I_{15/2} transitions of Er³⁺, respectively. Randomly oriented emitters in small spherical nanoparticles are generally regarded as a linear combination of incoherent dipoles aligned along the x, y, and z axes, leading to isotropic emission characteristics. In contrast, when coupling with anisotropic plasmonic structures, the excitation of a dipole moment with a specific orientation can be selectively enhanced by near-field interference, together with controlled decay dynamics, by adjusting the radiation properties of the plasmonic mode. Considering both the incident polarization angle and the dipole orientation, the polarization-dependent luminescence enhancement of an upconversion emitter in the vicinity of plasmonic antennas, which includes both excitation and emission processes, can be expressed as follows:

$$f_{total}^{\theta} = f_{ex}^{\theta} * f_{em}^{\theta} = \frac{|\boldsymbol{\mu} \cdot \mathbf{E}_{\theta}|^4 \gamma_T^0}{|\boldsymbol{\mu} \cdot \mathbf{E}_0|^4 \gamma_T^{\theta}} * \frac{\eta_{\theta}(\omega)}{\eta_0(\omega)} \quad (\text{Equation 1})$$

¹Department of Chemistry, National University of Singapore, Singapore 117543, Singapore

²Institute of Materials Research and Engineering, Agency for Science, Technology and Research, Singapore 138634, Singapore

³Singapore University of Technology and Design, Singapore 487372, Singapore

⁴Centre de Recherche Paul Pascal, University of Bordeaux, CNRS, Pessac 33600, France

⁵Lead contact

*Correspondence: renaud.vallee@crpp.cnrs.fr (R.A.L.V.), chmlx@nus.edu.sg (X.L.)

<https://doi.org/10.1016/j.chempr.2023.11.007>

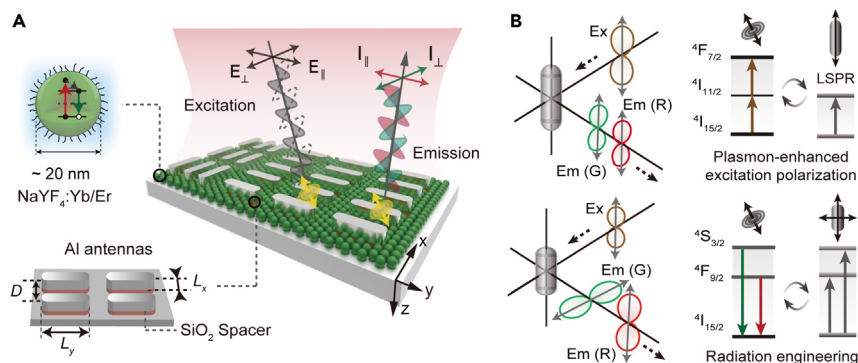


Figure 1. The design of plasmon-emitter hybrid nanostructures for precise control of upconversion luminescence polarization

(A) Schematic of the hybrid system comprising MIM nanoantennas and NaYF₄:Yb³⁺/Er³⁺ UCNPs. The hybrid system is composed of Al-rod-like antennas on a SiO₂ layer, surrounded by UCNPs. L_y and L_x represent the dimension of Al nanoantennas along the y axis and x axis, respectively. (B) Simplified energy level diagram (right) depicting how anisotropic gap-plasmon modes interact with the quantum energy levels of UCNPs. The modification of upconversion luminescence polarization depends on the localized surface plasmon resonance (LSPR) wavelength relative to the excitation (Ex) and emission (Em) transitions of UCNPs. This polarization modification arises from both plasmon-enhanced excitation polarization through near-field electromagnetic interference and plasmon-coupled emission through radiation engineering.

where μ is the electric transition of electric dipole moment and E_0 and E_θ represent the incident field and the polarization-dependent localized E-field, respectively, under plasmon resonance excitation. Accordingly, the polarization enhancement by plasmon excitation contains two competing contributions, including the positive contribution of the fourth power of near-field enhancement, $\frac{|\mu \cdot E_\theta|^4}{|\mu \cdot E_0|^4}$, and the negative contribution of the relaxation factors for the total decay rate of the intermediate state $\frac{\gamma_\theta^0}{\gamma_\theta^1}$. Meanwhile, the polarization-dependent radiation characteristics are determined by the antenna-modified quantum efficiency $\eta_\theta(\omega)$ at frequency ω , which is related to both local radiative and nonradiative processes. The symbol θ represents the orientation angle of the dipole source or the excitation polarization angle. To control the polarization states of emitters at the nanoscale, it is desirable to couple the polarization-dependent resonant modes with the pump field and the emitting transitions to achieve efficient excitation and radiation of photoluminescence.

Fabrication of UCNP-coupled plasmonic antennas

Based on theoretical considerations, we designed and fabricated the plasmon-emitter hybrid structure comprising periodic MIM nanostructures, Al rod/SiO₂/Al film, coupled with UCNPs around antennas (Figures 1A and S1). The rod-shaped Al nanoantennas with a silica spacer were fabricated above the Al film by electron beam lithography (Figure S2). The antenna surface has a native oxidation layer of Al₂O₃ (2–3 nm) to extend the durability of the antenna and serve as a spacer for nearby dipole emitters to minimize metal loss. Moreover, the metallic gap provides several orders of magnitude improvement in photoluminescence compared with antennas without the reflective layer.³⁹ A key advantage of Al-based gap mode plasmonic cavities is their ability to enable orthogonal resonant modes by adjusting their longitudinal (L_y) and transversal (L_x) lengths.^{32,37,40}

To decouple upconversion excitation and radiation processes, double-resonant plasmon modes were designed to coincide with the green emission of UCNPs in

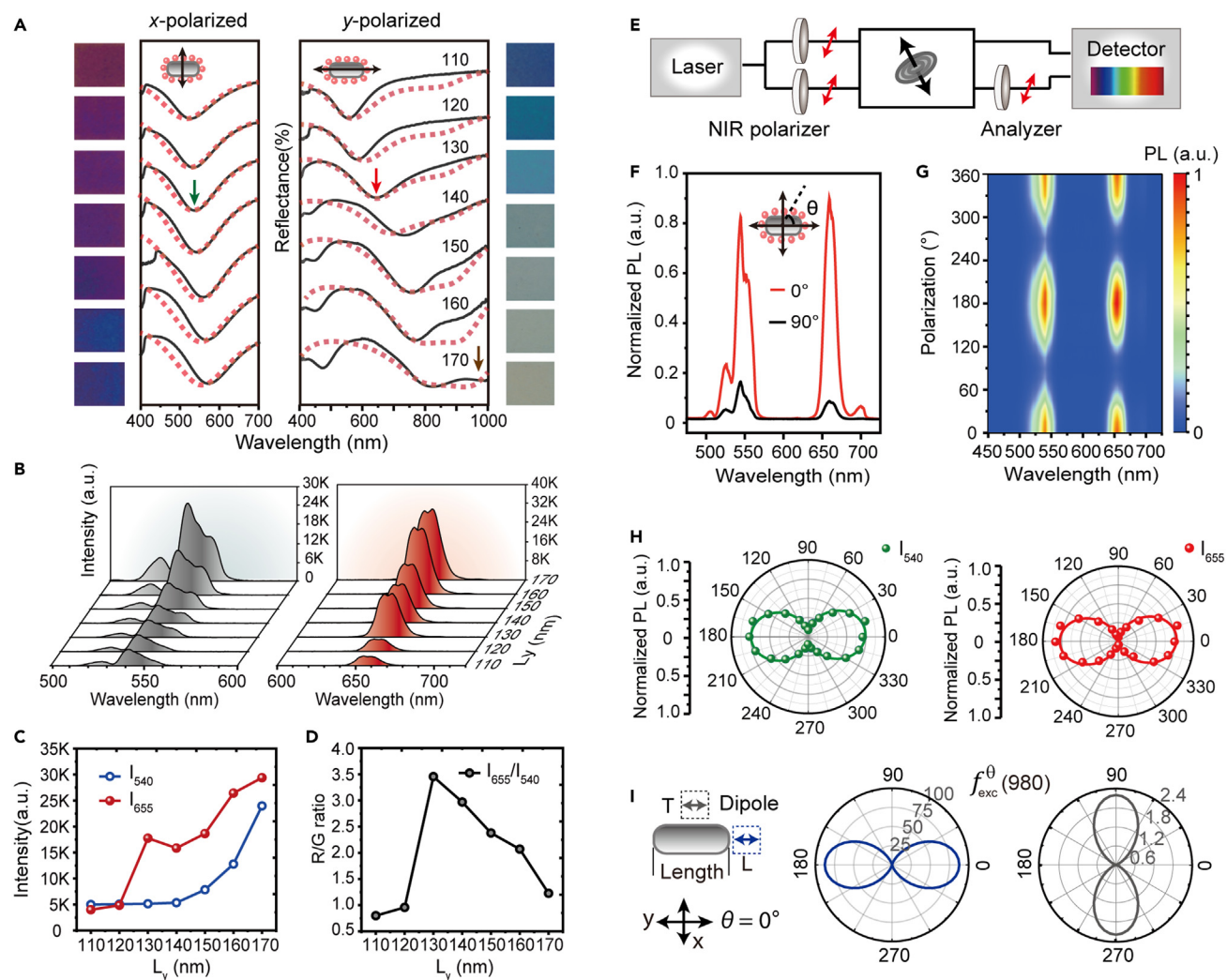


Figure 2. Polarization-dependent optical properties of plasmon-emitter hybrid nanostructures

(A) Optical images and reflectance spectra of the hybrid systems with varying L_y (rod length) from 110 to 170 nm, illuminated under y- and x-polarized incident broadband light. Black and red lines represent experimental and simulated reflection, respectively.

(B) Comparison of emission spectra for $\text{NaYF}_4:\text{Yb}^{3+}/\text{Er}^{3+}$ nanoparticles around MIM antennas with varying L_y from 110 to 170 nm.

(C) Upconversion luminescence intensities of green and red emission bands as a function of L_y .

(D) Red-to-green intensity ratios (I_{655}/I_{540}) as a function of L_y .

(E) Simplified schematic of upconversion polarization measurements.

(F) Experimental upconversion emission spectra of UCNPs coupled to antenna-170 for two laser excitation polarizations (parallel and perpendicular to the longitude y axis).

(G) Dependence of upconversion emission spectra on excitation polarization angle (θ).

(H) Polar plots of upconversion peak intensity as a function of excitation polarization angle (θ).

(I) Simulation results for polarization-dependent excitation enhancement factor (f_{exc}^θ) of dipole emitters located longitudinally (L) and transversally (T) with respect to rod antennas. The gray numbers marked on the polar pattern represent enhancement factors. The separation distance between the emitters and antennas is 5 nm.

the transversal direction (along the x axis) and either the red emission or excitation frequency in the longitudinal direction (along the y axis). Based on simulation results using the finite-difference time-domain (FDTD) method, we fabricated a series of biaxial rod antennas with L_x fixed at 95 nm and L_y varying from 110 to 170 nm. $\text{NaYF}_4:\text{Yb}^{3+}/\text{Er}^{3+}$ nanoparticles with a diameter of about 20 nm were synthesized and assembled around MIM structures (Figure S3). The reflection spectra of the fabricated structures were obtained under incident broadband light (Figure 2A),

which represents localized surface plasmon resonance (LSPR) arising from near-field interference between localized plasmons and incident light. At LSPR wavelength, the simulated local electric fields show plasmonic hot spots under both orthogonally polarized illuminations (Figure S4). According to reflection results, it was observed that the plasmon wavelength remained at approximately 540 nm in the transverse direction but could be adjusted from the visible to the near-infrared range in the longitudinal direction. This characteristic aligns well with the upconversion excitation and emission processes, facilitating effective enhancement of plasmon effects. Although L_x was fixed at 95 nm, the variations in the aspect ratio of the Al rod induced a change in localized electromagnetic fields with longer L_y . As a result, the plasmon resonance varied slightly in the transverse direction but continued to overlap with the green upconversion emission.

Evolution of upconversion luminescence by coupling with gap plasmon modes

A home-built optical microscope system was utilized to examine the coupling interaction between upconversion emitters and MIM nanostructures (Figure S5). We began by measuring a series of plasmon-enhanced upconversion luminescence without changing the excitation polarization. Under 980 nm excitation polarized along the y axis, both green and red upconversion emission bands showed a consistent trend of increased intensity as L_y increased, despite some fluctuations in the red band (Figures 2B and 2C). As L_x was fixed, the resonant mode remained coupled in a transverse direction with the green emission. When L_y was increased from 110 to 170 nm, the plasmon resonance gradually approached the excitation wavelength of the conversion process, leading to optimized excitation enhancement effects. As a result, the antenna with L_y of 170 nm can provide an effective enhancement effect for the longitudinal excitation process, indicating that the antenna with L_y of 170 nm is preferable for the decoupling of excitation and emission processes. The ratio of red-to-green intensity showed a distinctive trend resembling a volcano shape as L_y increased. The maximum ratio was observed in the sample with L_y measuring 130 nm. This suggests that the antenna with an L_y of 130 nm provides the most favorable enhancement effects on red emission in the longitudinal direction. Moreover, the anisotropic enhancement effects on both upconversion emissions lead to the maximum ratio between red and green emission (Figure 2D). This characteristic makes the antenna with an L_y of 130 nm an excellent choice for effectively separating and enhancing two orthogonal upconversion decay processes. These two antenna patterns were denoted as “antenna-130” and “antenna-170” for further polarization investigations (*vide infra*).

In lanthanide-mediated upconversion, long-lived intermediate excited states serve as energy reservoirs that sequentially populate higher-energy-emitting levels. The dependence of emission intensity (I) on excitation power density (P) can be expressed as ($I \propto P^n$) in the weak excitation regime, where n represents the number of upconversion steps involved.⁴¹ We measured power-dependent upconversion signals for UCNPs assembled on MIM nanostructures and Al film without nanoantennas (Figure S6). Results were plotted on a double-logarithmic scale, revealing a linear response to power density (Figure S7). Under 980 nm excitation, the slopes of green and red emissions from UCNPs on Al film were 1.52 and 1.90, respectively. In contrast, when UCNPs were coupled to the metasurface, the slopes of green emission decreased to 1.29 and 1.09 for antenna-130 and antenna-170 arrays, respectively, while the slopes of red emission decreased to 1.65 and 1.33, respectively. These findings suggest a significantly enhanced local electrical field that accelerates the saturation of the excited state in patterned samples.^{42,43} To investigate the pump power sensitivity of multiphoton upconversion in Yb³⁺/Er³⁺ co-doped

UCNPs, we developed a numerical population kinetic model involving two-photon populations (Figure S8). The results showed that the slope of the population evolution gradually decreased with higher pump rate. When an UCNP is placed near a plasmonic structure, the strong local electric field induced by the surface plasmon resonance can enhance the photon flux of excitation, leading to improved energy harvesting by sensitizer ions. Although the output power of the laser source remains constant, UCNPs embedded in the nanocavities are likely exposed to a much higher pumping photon flux, exciting Er^{3+} ions from the ground state to the emitting excited state more effectively. As a result, the plasmon hot spots accelerate multiphoton processes, which results in reduced slopes. Moreover, the plasmon enhancement factor is determined by the ratio of luminescence from particles coupled to plasmonic structures (I) to the luminescence intensity of bare particles without a pattern (I_0). We plotted the power-dependent enhancement factors by calculating I/I_0 (Figure S9). In the weak excitation regime, the enhancement effects are more pronounced due to multiphoton process. However, as the excitation pump increases, the intermediate energy level of the upconversion process gradually saturates, leading to less effective enhancement. The green and red emissions of UCNPs were 50- and 66-fold higher for the sample with antenna-170 than for particles without the metasurface, while they were 8- and 30-fold higher for the sample with antenna-130 (pump power: 1.47 mW; Figure S7).

Selective polarization modification of excited and radiative dynamics

We further verified the polarization responses of our hybrid platforms based on the optimized nanoantenna parameters and excitation power. Hybrid nanostructures were measured using polarization-resolved photoluminescence spectroscopy. Excitation-dependent polarization measurements were performed by tuning a near-infrared (NIR) polarization filter and a half-wave plate in front of the laser source, while anisotropic emission features were characterized by varying a polarization analyzer in front of the detector (Figures 2E and S5). In control experiments, we first measured the polarization-dependent luminescence of randomly oriented UCNPs on Al film (Figure S10). The upconversion luminescence remained almost unchanged under varied excitation. For particle-coupled metasurfaces, we defined the polarization direction as 0° for the excitation light polarized along the long rod axis (y axis). In the sample with UCNPs coupled to antenna-170 arrays, the detected upconversion luminescence intensity was found to fluctuate periodically, with a change in excitation polarization from 0° to 360° , resulting in a sinusoidal dependence on the polarization angle (Figures 2F and 2G). The maximum (I_{max}) and minimum (I_{min}) luminescence intensities occurred when excitation light was polarized parallel and perpendicular along the longitudinal axis of the nanoantennas, respectively. Polarization sensitivity can be quantitatively analyzed using the degree of polarization (DOP): $\text{DOP} = (I_{max} - I_{min}) / (I_{max} + I_{min})$. Calculated DOPs are up to 0.83 and 0.70 for red and green emission peaks, respectively, indicating that plasmon-enhanced upconversion luminescence has a strong polarization sensitivity to the excitation light (Figure 2H). Antenna-130 also demonstrated similar luminescence polarization dependence, but with relatively lower DOPs (red emission, 0.77, and green emission, 0.43; Figure S11), plausibly because the longitudinal resonance mode of antenna-130 is less optically matchable with the excitation wavelength of UCNPs.

We next used the FDTD method to simulate excitation enhancement factors (f_{ex}^θ) induced by localized resonance surface plasmons. Near-field patterns at the excitation wavelength of 980 nm were simulated in different excitation orientations (Figure S12). Rod-shaped antennas acted as optical concentrators that enabled both local-field confinement and polarization-controlled field rotation. Based on our

proposed modeling (Equation 1), the total f_{ex}^{θ} of plasmon-coupled upconversion emitters was simulated as a function of excitation orientation (Figure S13). Two representative positions were chosen for the investigation: the positions of emitters in the longitudinal (L) and transversal (T) directions with respect to the long axis of rod antennas (Figure 2). For the antenna-170 sample, the polar plots of f_{ex}^{θ} at L and T positions showed dipole patterns polarized along the y axis and x axis of rod antennas, respectively. Moreover, the enhancement factors at L position were numerically much larger than those at the T position, indicating that nanoparticles in the L regions mostly experience the plasmon-enhanced pump field. Thus, the total luminescence tends to obey the longitudinal polarization. The simulated polar excitation pattern of antenna-130 is similar to that of antenna-170 but shows relatively smaller enhancement factors (Figure S14). Our simulation analysis agreed well with experimental results of longitudinally polarized upconversion luminescence (Figure 2H), confirming that excitation polarization is due to the modified excitation transition induced by the actively tunable plasmon hotspots.

After selectively exciting the upconversion emitter by the enhanced near-field, we further considered how the decay channels of the emitter's exciton energy was modulated by the local density of photon states around the antennas. For optical measurements, luminescence emission was recorded by varying the polarization analyzer in front of the detector from 0° to 360° , whereas the polarization of the excitation laser was either parallel or perpendicular to the long axis of rod antennas. In the control experiments, the upconversion luminescence of randomly oriented UCNPs on Al film showed a nearly isotropic emission response at varied polarizer angles (Figure S10). In contrast, upconversion spectra showed a periodic variation as a function of emission polarization angle due to coupling to anisotropic plasmon modes (Figures 3A–3D). Polar plots can be well fitted with a cosine squared function. When the antenna-170 sample was excited in the longitudinal direction, the intensity of the red emission was greater than that of the green emission, but the two emissions were both longitudinally polarized (Figure 3A). Conversely, the intensity of the green emission became stronger than that of the red emission when excited in the transverse direction, while both emissions adopted the polarized behavior of plasmons and became polarized in the transverse direction (Figure 3B).

For the antenna-130 sample, the dual-resonance plasmon modes of antennas can selectively couple with the 655 nm emission longitudinally and the 540 nm emission transversally, decoupling polarization states of the green and red emission in orthogonal directions (Figures 3C and 3D). The two emission bands showed distinct variations as a function of the polarization angle of the emission. For longitudinal excitation, the polar plot of the emission at 655 nm was polarized along the y axis of antennas, corresponding to the case of antenna-170 (Figure 3C). Conversely, the polar plot of the 540 nm emission was polarized along the x axis of antennas. With transverse excitation, the red and green emissions retained the polarization features in perpendicular directions, but the green emission became stronger than the red (Figure 3D).

To elucidate how the geometrical engineering of the Al-rod nanoantennas influences the polarization responses of the radiation process, we simulated plasmon-modified radiative decay dynamics (Figure 3E). The emission enhancement (f_{em}) of an emitter has two contributors: decay rate enhancement (Purcell factor, F_{rad}) and antenna-accelerated efficiency (η_{a}).³⁹ Figure 3E shows the polar plots of f_{em}^{θ} as a function of dipole orientation θ for two characteristic wavelengths. For the antenna-170 sample, the dependencies of f_{em}^{θ} (655 nm) and f_{em}^{θ} (540 nm) were mainly polarized

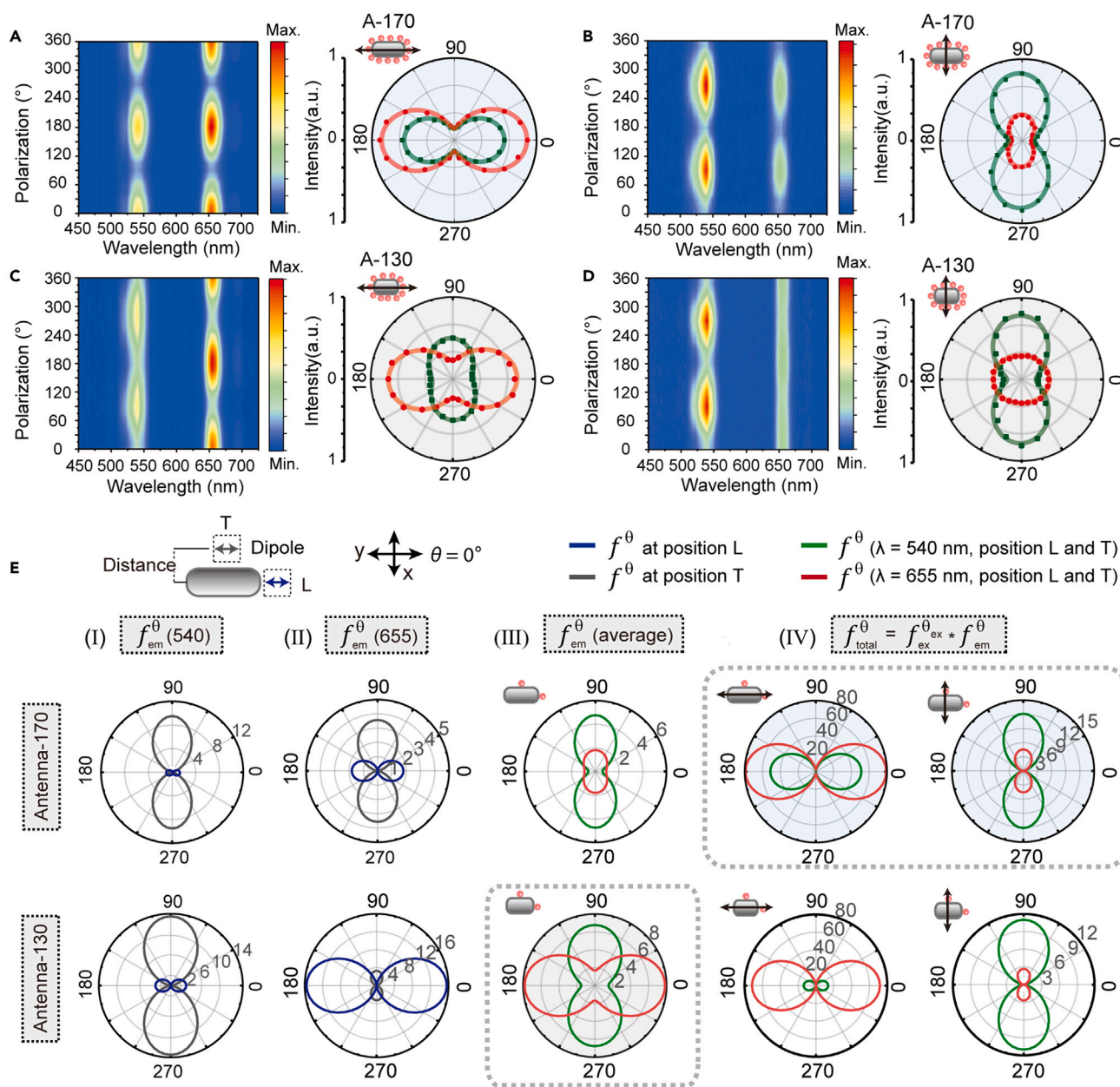


Figure 3. Upconversion luminescence with programmable multicolor emission and polarization states

(A and B) Upconversion emission variation and the corresponding peak intensity polar plot as a function of emission polarization angle for the antenna-170 sample. The excitation is oriented in the longitude direction (A) and transverse direction (B), respectively.

(C and D) Upconversion emission variation and corresponding peak intensity polar plot as a function of emission polarization angle for the antenna-130 sample. The excitation is oriented in the longitude direction (C) and transverse direction (D), respectively.

(E) Simulations of polarization-dependent emission enhancement factors (f_{em}^θ) for dipole emitters located longitudinally (L) and transversally (T) with respect to rod antennas (column I and column II). Simulations of polarization-dependent average emission enhancement factors, $f_{em}^\theta(\text{average})$, and total enhancement factors (f_{total}^θ) for dipole emitters with the emission wavelength at 540 and 655 nm (column III and column IV). The gray numbers on the polar pattern represent enhancement factors. The separation distance between the emitters and antennas is set to 5 nm. The polar pattern of $f_{em}^\theta(\text{average})$ was plotted by calculating the average value of f_{em}^θ at T and L locations, $f_{em}^\theta(\text{average}) = \frac{f_{em}^\theta(L) + f_{em}^\theta(T)}{2}$, which showed a dominant polarization state along the transverse direction for the sample of antenna-170 and showed obvious anisotropic polarization properties in orthogonal directions for the sample of antenna-130. The total enhancement factors (f_{total}^θ) were calculated by integrating excitation and emission enhancements in both T and L positions, $f_{total}^\theta = \frac{f_{total}^\theta(L) + f_{total}^\theta(T)}{2}$. The symbol θ represents the orientation angle of the dipole source. θ_{ex} represents the excitation polarization angle.

transversely due to resonance coupling at position T. This means that transverse polarization can effectively boost both green and red emissions. In contrast, for antenna-130, the polar plot of f_{em}^{θ} (655 nm) at position L is largely polarized in the longitudinal direction, while f_{em}^{θ} (540 nm) at position T is much more polarized in the transverse direction. As a result, the f_{em}^{θ} polar pattern of red emission is predominantly polarized in the longitudinal direction, while the green emission is polarized in the transverse direction. This anisotropic enhancement effect thus allowed selective modification of the polarization of different spectral components in UCNPs by near-field anisotropic techniques. These results suggest that antenna-130 is best suited to efficiently decouple two upconversion radiation channels into orthogonal polarization directions.

The total emission polarization originates from the synergistic effect of the plasmon-enhanced excitation polarization and the plasmon-coupled decay process. Thus, the upconversion polarization behaviors may vary depending on the synergistic effects of the excitation and emission enhancement. Meanwhile, polarization signals from the emitters distributed outside specific areas (T and L positions) change the final polarization patterns. To exploit the synergistic effects on polarization modification, we consider two extreme situations in theory (e.g., excitation-dominated or emission-dominated conditions) and conduct a comparative analysis with the experimental measurements. In the situation where the emission manipulation dominates, the excitation interference would be neglected. We directly plotted the polar pattern of f_{em}^{θ} (average) by calculating the average value of f_{em}^{θ} at both T and L positions (Figure 3E). For the sample of antenna-170, f_{em}^{θ} (average) showed a dominant polarization state along the transverse direction, while f_{em}^{θ} (average) for the sample of antenna-130 showed obvious anisotropic polarization properties in orthogonal directions. Moreover, the selective manipulation of the excitation by active tuning of plasmonic hotspots was considered (Figures 2I and S14). After combining the excitation enhancement factors, the total enhancement factors (f_{total}^{θ}) of antenna-170 showed a polar pattern that varied with excitation orientation. The polarization directions remain fairly consistent with the experimental results of antenna-170 (Figures 3A and 3B). In this situation, the longitudinal resonance mode coincides well with the excitation light at 980 nm, leading to a theoretically large excitation enhancement factor (the maximum value of 87.7 for f_{ex}^{θ} ; Figure 2I). Although the simulated f_{em}^{θ} shows a dominant polarization state along the transverse direction, it is much lower than f_{ex}^{θ} , indicating that the excitation resonance is much more crucial for photon-plasmon coupling in this case and thus imparts upconversion luminescence with parallel polarized features inherited from the dominant excitation coupling (Figures 3A and 3B). For the antenna-130 sample, the total enhancement factors (f_{total}^{θ}) after combining the excitation manipulation also showed a polar pattern that varied with the excitation orientation (Figure 3E).

However, in experiments, the plasmon-coupled upconversion emitters exhibited anisotropic properties regardless of whether the laser excitation was perpendicular or parallel to the long axis of the rod antenna (Figures 3C and 3D). In contrast, the experimental polarization results of antenna-130 closely matched the simulated polar pattern of f_{em}^{θ} (average) rather than the total enhancement effects, suggesting that the emission manipulation was indeed dominant. This is because, in the case of the 130 nm antennas, the decomposed f_{em}^{θ} is comparable or even slightly larger than f_{ex}^{θ} (the maximum value of 15.6 for f_{em}^{θ} and 9.7 for f_{ex}^{θ}) (Figures 3E and S14), indicating that the effect of emission enhancement has the potential to overcome the excitation interference. The relatively lower ability of antenna-130 to manipulate excitation may lead to a situation where emission manipulation dominates. However, it is noted

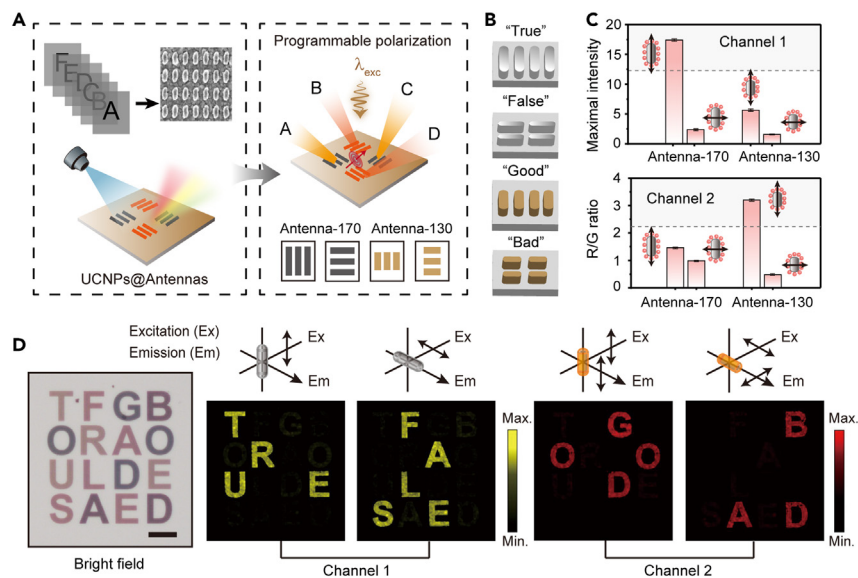


Figure 4. Polarization-controlled upconversion multiplexing

(A) Schematic showing the information coding by patterning antenna-170 and antenna-130 in orthogonal directions. The hidden information can be decoded by switching the excitation or the detection polarization angles.

(B) An image pattern composed of four sets of English characters, which are fabricated using UCNP-coupled antenna-170 and antenna-130 in orthogonal directions.

(C) The maximal luminescence intensity and red-to-green (R/G) emission ratio obtained from antenna-170 and antenna-130 samples, demonstrating that distinct image patterns can be resolved by imaging luminescence intensity (channel 1) and differentiating emission ratiometry (channel 2).

(D) Bright field, upconversion luminescence intensity (channel 1) and R/G-ratiometric (channel 2) imaging of UCNP-coupled plasmon patterns. Image patterns can be programmed by switching the excitation or the detection polarization angles. Scale bars, 30 μm .

that the experimental green polar pattern under longitudinal excitation and the red polar pattern under transverse excitation exhibit a much lower DOP, which may be caused by the excitation interference. Although the polarization direction did not change, the shape of the polar pattern was obviously modified. Notably, there are some differences between the numerical results and the measured enhancement factor, which are due to the imperfect dielectric environment in the plasmonic cavity and the complicated multiphoton processes in the ESA-mediated theoretical model.

To examine the distance effect on enhancement factors, the same simulations were performed for the emitters located at a distance of 10 nm from the rod antennas (Figures S15–S17). The simulated results showed a similar enhancement pattern compared with those with 5 nm spacing (Figure 3E). However, the numerical enhancement factors are completely lower than the corresponding value in a nearby case. The results indicate that the value of the total enhancement factors changes as a function of distance, but the effects on the polarized emission remained similar. Therefore, the dominant features, such as the emitting wavelengths and polarization states, should remain the same.

Programmable upconversion multiplexing

Taking advantage of the polarization-controlled multi-level upconversion response, we demonstrated a scheme for optical information multiplexing in different frequencies and polarizations using our plasmon-emitter system (Figures 4A and 4B). Polarization-dependent luminescence intensity imaging and luminescence

ratiometry were used as two channels to transmit distinct information. The polarization alignment (e.g., the excitation orientation and the detection polarization angle) was used as the key to decode the information. Multiplexed information can be resolved by selecting the thresholds for both intensity and ratiometry by comparing luminescence intensity and red-to-green emission ratiometry in antenna-170 and antenna-130 samples (Figure 4C). To demonstrate the concept, four words were constructed by coupling antenna-170 and antenna-130 orthogonally, resulting in 16 letters hidden in the image (Figure 4D). It is possible to resolve TRUE and FALSE words by imaging luminescence intensity and interconverting them by altering the polarization of the incident wave (Figure 4D). The emission ratiometry can be used to differentiate between two other words (GOOD and BAD), based on different excitation and detection polarization angles.

Conclusions

Our experimental data and simulations have shown that anisotropic plasmon engineering offers a solution to surpass the constraints of crystalline symmetry in isotropic upconversion nanocrystals, enabling multi-level polarized upconverted signals. By precisely modulating the optical density of states in subwavelength gap-mode-supported metasurfaces, we have achieved effective control over the population kinetics for nonlinear light generation. This control allows us to actively manipulate the emission intensity, frequency, and polarization states of upconversion luminescence. Our investigations provide valuable insights into the design principles for advanced nonlinear quantum systems, offering tailored frequency and polarization behavior at the nanoscale. This study opens up new possibilities in nanoscale light polarization control, with potential applications including all-optical integrated circuits, polarized color generation for optical security and pattern display, polarized light-emitting diodes, and ultrasensitive polarimetry.^{37,44,45}

EXPERIMENTAL PROCEDURES

Resource availability

Lead contact

Further information and requests for resources should be directed to and will be fulfilled by the lead contact, Professor Xiaogang Liu (chmlx@nus.edu.sg).

Materials availability

This study did not generate new materials.

Data and code availability

This study did not generate any datasets.

Methods

Full experimental and simulation procedures are provided in the [supplemental information](#).

SUPPLEMENTAL INFORMATION

Supplemental information can be found online at <https://doi.org/10.1016/j.chempr.2023.11.007>.

ACKNOWLEDGMENTS

This work is supported by the Agency for Science, Technology and Research (A*STAR) (grant no. A1983c0038, Career Development fund no. C222812011 and SC25/22-821314) and National Research Foundation, Prime Minister's Office,

Singapore, under its Competitive Research Program (CRP award no. NRF-NRFI05-2019-0003).

AUTHOR CONTRIBUTIONS

J.X. designed the experiments. H.L., Hongtao Wang, and Hao Wang fabricated plasmon structures. J.X., Y.W., H.L., and B.Y.H.T. conducted the optical characterization. R.A.L.V. and J.X. performed theoretical simulations. X.L., J.K.W.Y., and R.A.L.V. supervised the project and led the collaboration efforts. J.X., Y.W., and X.L. analyzed the results and wrote the manuscript, with input from all authors.

DECLARATION OF INTERESTS

The authors declare no competing interests.

Received: June 10, 2023

Revised: October 1, 2023

Accepted: November 20, 2023

Published: December 14, 2024

REFERENCES

1. Fernandez-Bravo, A., Wang, D., Barnard, E.S., Teitelboim, A., Tajon, C., Guan, J., Schatz, G.C., Cohen, B.E., Chan, E.M., Schuck, P.J., et al. (2019). Ultralow-threshold, continuous-wave upconverting lasing from subwavelength plasmons. *Nat. Mater.* **18**, 1172–1176.
2. Tang, J., Xia, J., Fang, M., Bao, F., Cao, G., Shen, J., Evans, J., and He, S. (2018). Selective far-field addressing of coupled quantum dots in a plasmonic nanocavity. *Nat. Commun.* **9**, 1705.
3. Kim, M., Ko, S.M., Kim, J.M., Son, J., Lee, C., Rhim, W.K., and Nam, J.M. (2018). Dealloyed intra-nanogap particles with highly robust, quantifiable surface-enhanced Raman scattering signals for biosensing and bioimaging applications. *ACS Cent. Sci.* **4**, 277–287.
4. Wei, J., Xu, C., Dong, B., Qiu, C.W., and Lee, C. (2021). Mid-infrared semimetal polarization detectors with configurable polarity transition. *Nat. Photonics* **15**, 614–621.
5. Gai, S., Li, C., Yang, P., and Lin, J. (2014). Recent progress in rare earth micro/nanocrystals: soft chemical synthesis, luminescent properties, and biomedical applications. *Chem. Rev.* **114**, 2343–2389.
6. Kim, J., Chacón, R., Wang, Z., Larquet, E., Lahlil, K., Leray, A., Colas-des-Francis, G., Kim, J., and Gacoin, T. (2021). Measuring 3D orientation of nanocrystals via polarized luminescence of rare-earth dopants. *Nat. Commun.* **12**, 1943.
7. Zheng, X., Kankala, R.K., Liu, C.G., Wen, Y., Wang, S., Bin, C., A.Z., and Zhang, Y. (2022). Tailoring lanthanide upconversion luminescence through material designs and regulation strategies. *Adv. Opt. Mater.* **10**, 2200167.
8. Wen, S., Zhou, J., Zheng, K., Bednarkiewicz, A., Liu, X., and Jin, D. (2018). Advances in highly doped upconversion nanoparticles. *Nat. Commun.* **9**, 2415.
9. Richards, B.S., Hudry, D., Busko, D., Turshatov, A., and Howard, I.A. (2021). Photon upconversion for photovoltaics and photocatalysis: A critical review. *Chem. Rev.* **121**, 9165–9195.
10. Wu, Y., Xu, J., Qin, X., Xu, J., and Liu, X. (2021). Dynamic upconversion multicolour editing enabled by molecule-assisted opto-electrochemical modulation. *Nat. Commun.* **12**, 2022.
11. Wu, Y., Chan, S.Y., Xu, J., and Liu, X. (2021). Multiphoton upconversion materials for photocatalysis and environmental remediation. *Chem. Asian J.* **16**, 2596–2609.
12. Duan, R., Xu, Y., Zeng, X., Xu, J., Liang, L., Zhang, Z., Wang, Z., Jiang, X., Xing, B., Liu, B., et al. (2021). Uncovering the metabolic origin of aspartate for tumor growth using an integrated molecular deactivator. *Nano Lett.* **21**, 778–784.
13. Zheng, W., Huang, P., Tu, D., Ma, E., Zhu, H., and Chen, X. (2015). Lanthanide-doped upconversion nano-bioprobes: electronic structures, optical properties, and biodetection. *Chem. Soc. Rev.* **44**, 1379–1415.
14. Liu, Q., Zhang, Y., Peng, C.S., Yang, T., Joubert, L.M., and Chu, S. (2018). Single upconversion nanoparticle imaging at sub-10 W cm⁻² irradiance. *Nat. Photonics* **12**, 548–553.
15. Deng, R., Qin, F., Chen, R., Huang, W., Hong, M., and Liu, X. (2015). Temporal full-colour tuning through non-steady-state upconversion. *Nat. Nanotechnol.* **10**, 237–242.
16. Dong, H., Sun, L.D., Feng, W., Gu, Y., Li, F., and Yan, C.H. (2017). Versatile spectral and lifetime multiplexing nanoplatform with excitation orthogonalized upconversion luminescence. *ACS Nano* **11**, 3289–3297.
17. Pei, P., Chen, Y., Sun, C., Fan, Y., Yang, Y., Liu, X., Lu, L., Zhao, M., Zhang, H., Zhao, D., et al. (2021). X-ray-activated persistent luminescence nanomaterials for NIR-II imaging. *Nat. Nanotechnol.* **16**, 1011–1018.
18. Tan, M., Li, F., Wang, X., Fan, R., and Chen, G. (2020). Temporal multilevel luminescence anticounterfeiting through scattering media. *ACS Nano* **14**, 6532–6538.
19. Das, A., Mao, C., Cho, S., Kim, K., and Park, W. (2018). Over 1000-fold enhancement of upconversion luminescence using water-dispersible metal-insulator-metal nanostructures. *Nat. Commun.* **9**, 4828.
20. Zhou, D., Liu, D., Xu, W., Yin, Z., Chen, X., Zhou, P., Cui, S., Chen, Z., and Song, H. (2016). Observation of considerable upconversion enhancement induced by Cu₂S plasmon nanoparticles. *ACS Nano* **10**, 5169–5179.
21. Lu, D., Cho, S.K., Ahn, S., Brun, L., Summers, C.J., and Park, W. (2014). Plasmon enhancement mechanism for the upconversion processes in NaYF₄:Yb³⁺,Er³⁺ nanoparticles: Maxwell versus Förster. *ACS Nano* **8**, 7780–7792.
22. Debasu, M.L., Ananias, D., Pastoriza-Santos, I., Liz-Marzán, L.M., Rocha, J., and Carlos, L.D. (2013). All-in-one optical heater-thermometer nanoplatform operative from 300 to 2000 K based on Er³⁺ emission and blackbody radiation. *Adv. Mater.* **25**, 4868–4874.
23. Wang, Y., Zheng, K., Song, S., Fan, D., Zhang, H., and Liu, X. (2018). Remote manipulation of upconversion luminescence. *Chem. Soc. Rev.* **47**, 6473–6485.
24. Chen, H., Jiang, Z., Hu, H., Kang, B., Zhang, B., Mi, X., Guo, L., Zhang, C., Li, J., Lu, J., et al. (2022). Sub-50-ns ultrafast upconversion luminescence of a rare-earth-doped nanoparticle. *Nat. Photonics* **16**, 651–657.
25. Meng, Y., Huang, D., Li, H., Feng, X., Li, F., Liang, Q., Ma, T., Han, J., Tang, J., Chen, G., et al. (2023). Bright single-nanocrystal upconversion at sub 0.5 W cm⁻² irradiance via coupling to single nanocavity mode. *Nat. Photonics* **17**, 73–81.
26. Kim, J., Michelin, S., Hilbers, M., Martinelli, L., Chaudan, E., Amselem, G., Fradet, E., Boilot,

- J.P., Brouwer, A.M., Baroud, C.N., et al. (2017). Monitoring the orientation of rare-earth-doped nanorods for flow shear tomography. *Nat. Nanotechnol.* **12**, 914–919.
27. Zhou, J., Chen, G., Wu, E., Bi, G., Wu, B., Teng, Y., Zhou, S., and Qiu, J. (2013). Ultrasensitive polarized up-conversion of Tm^{3+} – Yb^{3+} doped β - NaYF_4 single nanorod. *Nano Lett.* **13**, 2241–2246.
28. Huang, L., Zhao, Y., Zhang, H., Huang, K., Yang, J., and Han, G. (2017). Expanding anti-stokes shifting in triplet-triplet annihilation upconversion for in vivo anticancer prodrug activation. *Angew. Chem. Int. Ed.* **129**, 14592–14596.
29. Chen, L., Rong, Y., Ren, M., Wu, W., Qin, M., Pan, C., Ma, Q., Liu, S., Wu, B., Wu, E., et al. (2018). Selective polarization modification of upconversion luminescence of $\text{NaYF}_4:\text{Yb}^{3+}, \text{Er}^{3+}$ nanoparticles by plasmonic nanoantenna arrays. *J. Phys. Chem. C* **122**, 15666–15672.
30. Wu, Y., Xu, J., Poh, E.T., Liang, L., Liu, H., Yang, J.K.W., Qiu, C.W., Vallée, R.A.L., and Liu, X. (2019). Upconversion superburst with sub-2 μs lifetime. *Nat. Nanotechnol.* **14**, 1110–1115.
31. Xu, J., Dong, Z., Asbahi, M., Wu, Y., Wang, H., Liang, L., Ng, R.J.H., Liu, H., Vallée, R.A.L., Yang, J.K.W., et al. (2021). Multiphoton upconversion enhanced by deep subwavelength near-field confinement. *Nano Lett.* **21**, 3044–3051.
32. Liu, H., Xu, J., Wang, H., Liu, Y., Ruan, Q., Wu, Y., Liu, X., and Yang, J.K.W. (2019). Tunable resonator-upconverted emission (TRUE) color printing and applications in optical security. *Adv. Mater.* **31**, e1807900.
33. Rodrigues, S.P., Cui, Y., Lan, S., Kang, L., and Cai, W. (2015). Metamaterials enable chiral-selective enhancement of two-photon luminescence from quantum emitters. *Adv. Mater.* **27**, 1124–1130.
34. He, H., Cen, M., Wang, J., Xu, Y., Liu, J., Cai, W., Kong, D., Li, K., Luo, D., Cao, T., et al. (2022). Plasmonic chiral metasurface-induced upconverted circularly polarized luminescence from achiral upconversion nanoparticles. *ACS Appl. Mater. Interfaces* **14**, 53981–53989.
35. He, J., Zheng, W., Ligmajer, F., Chan, C.F., Bao, Z., Wong, K.L., Chen, X., Hao, J., Dai, J., Yu, S.F., et al. (2017). Plasmonic enhancement and polarization dependence of nonlinear upconversion emissions from single gold nanorod@ SiO_2 @ $\text{CaF}_2:\text{Yb}^{3+}, \text{Er}^{3+}$ hybrid core-shell-satellite nanostructures. *Light Sci. Appl.* **6**, 16217.
36. Kang, F., He, J., Sun, T., Bao, Z.Y., Wang, F., and Lei, D.Y. (2017). Plasmonic dual-enhancement and precise color tuning of gold nanorod@ SiO_2 coupled core-shell-shell upconversion nanocrystals. *Adv. Funct. Mater.* **27**, 1701842.
37. Goh, X.M., Zheng, Y., Tan, S.J., Zhang, L., Kumar, K., Qiu, C.W., and Yang, J.K.W. (2014). Three-dimensional plasmonic stereoscopic prints in full colour. *Nat. Commun.* **5**, 5361.
38. Liu, X., and Yuan Lei, D.Y. (2015). Simultaneous excitation and emission enhancements in upconversion luminescence using plasmonic double-resonant gold nanorods. *Sci. Rep.* **5**, 15235.
39. Fernandez-Garcia, R., Rahmani, M., Hong, M., Maier, S.A., and Sonnefraud, Y. (2013). Use of a gold reflecting-layer in optical antenna substrates for increase of photoluminescence enhancement. *Opt. Express* **21**, 12552–12561.
40. Langhammer, C., Schwind, M., Kasemo, B., and Zorić, I. (2008). Localized surface plasmon resonances in aluminum nanodisks. *Nano Lett.* **8**, 1461–1471.
41. Suyver, J.F., Aebischer, A., Garcia-Revilla, S., Gerner, P., and Güdel, H.U. (2005). Anomalous power dependence of sensitized upconversion luminescence. *Phys. Rev. B* **71**, 1098–10121.
42. Zhang, W., Ding, F., and Chou, S.Y. (2012). Large enhancement of upconversion luminescence of $\text{NaYF}_4:\text{Yb}^{3+}/\text{Er}^{3+}$ nanocrystal by 3D plasmonic nano-antennas. *Adv. Mater.* **24**, OP236–OP241.
43. Liang, L., Teh, D.B.L., Dinh, N.D., Chen, W., Chen, Q., Wu, Y., Chowdhury, S., Yamanaka, A., Sum, T.C., Chen, C.H., et al. (2019). Upconversion amplification through dielectric superlensing modulation. *Nat. Commun.* **10**, 1391.
44. Matioli, E., Brinkley, S., Kelchner, K.M., Hu, Y.L., Nakamura, S., DenBaars, S., Speck, J., and Weisbuch, C. (2012). High-brightness polarized light-emitting diodes. *Light Sci. Appl.* **1**, e22–e22.
45. Yuan, H., Liu, X., Afshinmanesh, F., Li, W., Xu, G., Sun, J., Lian, B., Curto, A.G., Ye, G., Hikita, Y., et al. (2015). Polarization-sensitive broadband photodetector using a black phosphorus vertical p-n junction. *Nat. Nanotechnol.* **10**, 707–713.